Thermodynamics of the Hubbard model on stacked honeycomb and square lattices

Journal Article

Author(s):
Imriška, Jakub; Gull, Emanuel; Troyer, Matthias

**THE EUROPEAN
PHYSICAL JOURNAL B**

Regular Article

Thermodynamics of the Hubbard model on stacked honeycomb and square lattices[*]

Jakub Imriška[1,a], Emanuel Gull[2], and Matthias Troyer[1]

[1] Theoretische Physik, ETH Zurich, 8093 Zurich, Switzerland
[2] Department of Physics, University of Michigan, Ann Arbor, MI 48109, USA

Abstract. We present a numerical study of the Hubbard model on simply stacked honeycomb and square lattices, motivated by a recent experimental realization of such models with ultracold atoms in optical lattices. We perform simulations with different interlayer coupling and interaction strengths and obtain Néel transition temperatures and entropies. We provide data for the equation of state to enable comparisons of experiments and theory. We find an enhancement of the short-range correlations in the anisotropic lattices compared to the isotropic cubic lattice, in parameter regimes suitable for the interaction driven adiabatic cooling.

1 Introduction

The single-orbital Hubbard model, originally introduced to describe correlation driven metal-insulator transitions [1], has been the subject of intensive study in recent years, as it is widely believed that its realization on a two-dimensional square lattice captures many of the salient features of high-temperature superconductivity [2,3]. Apart from a Fermi liquid phase at weak interaction and large doping strength and a correlation driven insulating phase at half filling and large interaction strength, superconducting phases of various types [4–7], pseudogap behavior in the absence of long-range order [8–11], ferromagnetic [12–14], and antiferromagnetic [15] phases, as well as different types of stripe phases [16,17] have been proposed.

Theoretical and numerical studies of the low temperature properties of the Hubbard model have proven to be difficult, especially in the strongly correlated regime where the interaction strength is comparable to the bandwidth and many low-lying degrees of freedom compete. Experimental realizations using cold atomic gas systems [18,19], on various lattices in two and three dimensions, offer an alternative route to increase our understanding the physics of this model. While the temperatures accessible by these experiment are still far above the superconducting phase transitions, a range of phenomena, including long range antiferromagnetic order in three dimensions, may soon be accessible [20–24].

One of the current challenges is the calibration of the precise parameters of experiments using ultracold atomic gases, and in particular their temperature or entropy. Numerical simulations of the model for a range of parameters have proven to be useful in this context, and especially quantities that show a strong dependence on temperature and are accessible both in simulation and experiment. An example are nearest neighbor the spin-correlations [22]. Comparison to numerics was able to identify unexpected heating effects and could pinpoint the temperature down to which the experimental realization of the model was accurate [23].

Motivated by the physics of graphene and by the search for a spin liquid state at low temperature [25–27], experimental realizations of the model on a honeycomb geometry have appeared [28] and provided results in agreement with numerical calculations of the 2d model [29,30]. Complementary to studies on isotropic lattices, anisotropic lattices of various types, e.g. with couplings in the vertical axis chosen differently from in-plane couplings, can be realized [22,28]. These models offer the possibility of studying a dimensional crossover between three, two and one dimensions and with this the possibility of tuning phase transitions to a more readily accessible regime.

From the experimental perspective, layered systems are a natural setup to investigate quasi-2d physics. The reduced dimensionality may give rise to interesting phenomena, but the presence of the third dimension will affect some of the low temperature properties – e.g. allowing for long range order at non-zero temperature which is absent in systems with continuous symmetries in two dimensions [31,32].

For the purpose of quantitative comparisons to cold atoms experiments, numerical simulations need to provide results at comparatively high temperature. For much

---
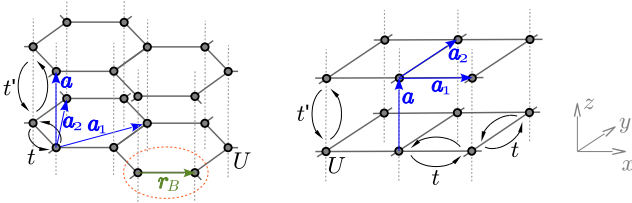
Fig. 1. Left panel: simply stacked honeycomb lattice with interaction U, in-plane hopping t, and inter-plane hopping t'. The dashed ellipse denotes the unit cell, containing two sites, A and B. The intracell vector $\mathbf{r}_B$ is displayed in green, $\mathbf{r}_A$ (not shown) is $\mathbf{0}$. The lattice basis vectors $\mathbf{a}_i$ are shown as blue arrows. Right panel: stacked square lattice. Here, the unit cell consists of a single site.

of the parameter regime accessible to experiment, high temperature series expansion and numerical linked cluster expansions seem to be sufficient. As the temperature is lowered outside of the convergence radius of these series, non-perturbative techniques are required. Cluster dynamical mean field methods in particular [33] are able to reach lower temperature in the thermodynamic limit both at and away from half filling and have been shown to be a reliable tool for this task [34].

Here we use these methods to study weakly to moderately coupled stacked honeycomb and square lattices, as depicted in Figure 1. The Hamiltonian of the Hubbard model on these lattices is

$$
\hat{H} = -t \sum_{\langle i,j \rangle, \sigma} \hat{c}_{i\sigma}^\dagger \hat{c}_{j\sigma} - t' \sum_{\langle i,j \rangle', \sigma} \hat{c}_{i\sigma}^\dagger \hat{c}_{j\sigma}
$$
$$
- \mu \sum_{i,\sigma} \hat{n}_{i\sigma} + U \sum_i \hat{n}_{i\uparrow} \hat{n}_{i\downarrow}, \tag{1}
$$

where $\hat{c}_{i\sigma}^\dagger$ ($\hat{c}_{i\sigma}$) creates (annihilates) a fermion at site i with spin $\sigma \in \{\uparrow, \downarrow\}$; $\hat{n}_{i\sigma} \equiv \hat{c}_{i\sigma}^\dagger \hat{c}_{i\sigma}$ denotes the occupation number operator, $U \geq 0$ is the repulsive on-site interaction, t the nearest-neighbor in-plane hopping, t' the interlayer hopping, and μ the chemical potential. By $\langle i,j \rangle$ we denote nearest neighbors i, j within a plane and by $\langle i,j \rangle'$ nearest neighbor pairs in adjacent planes.

We investigate the case $t \geq t' \geq 0$. Both lattices are bipartite and the model is thus particle-hole symmetric with half filling corresponding to $\mu = U/2$. The simply stacked square lattice in the regime of weakly coupled chains, $t' \geq t \geq 0$, was studied in reference [23]. Note that this simply stacked honeycomb lattice does not correspond to the lattice of graphite, where adjacent layers are shifted relative to each other.

The non-interacting bandwidth of the studied lattices is $W = 2Z_t t + 4t'$, where Z_t denotes the in-plane coordination number $Z_t = 3$ for the stacked honeycomb lattice, and $Z_t = 4$ for the stacked square lattice.

2 Method

We use the dynamical cluster approximation (DCA) method [35] to simulate the Hubbard model on both lat-

tices. DCA is a cluster extensions of the dynamical mean-field theory (DMFT) [33,36], systematically approaching the exact solution in the thermodynamic limit with growing cluster size. DCA self-consistently maps the lattice problem onto a cluster and approximates the lattice self energy by patch-wise constant self energy equal to the cluster self energy at the cluster reciprocal points. The stacked square lattice has a single site per unit cell and may be simulated by the standard DCA method. The simply stacked honeycomb lattice is simulated by a generalization of DCA formulated for an ℓ-site unit cell, which is explained in detail in Section 2.2.

For simulations of the paramagnetic phase we use the two-site unit cell depicted in the left panel of Figure 1. The basis vectors of the simply stacked honeycomb lattice are $\mathbf{a}_1 = \left(\frac{3}{2}, \frac{\sqrt{3}}{2}, 0 \right)$, $\mathbf{a}_2 = (0, \sqrt{3}, 0)$, $\mathbf{a}_3 = (0, 0, 1)$, and the intracell vectors are $\mathbf{r}_A = \mathbf{0}$, $\mathbf{r}_B = (1, 0, 0)$. The basis vectors of the stacked square lattice are the unit vectors in x, y, and z direction, $\mathbf{a}_1 = (1, 0, 0)$, $\mathbf{a}_2 = (0, 1, 0)$, $\mathbf{a}_3 = (0, 0, 1)$.

We locate the temperature of the Néel phase transition by measuring the divergence of the antiferromagnetic susceptibility. We found this method to be superior to allowing for translational symmetry breaking by doubling the unit cell and measuring the staggered magnetization directly. The reason is a critical slowing down of the DCA self-consistency loop close to the phase transition. Details are presented in Appendix A.

Most of the clusters utilized in the study respect the three-fold (four-fold) rotational symmetry around the vertical axis of the stacked honeycomb (square) lattice. The aspect ratio of the clusters is chosen to be similar to the anisotropy t/t'. Since non-bipartite clusters may cause artificial frustration at low temperature, we used them only for equation of state (EOS) calculations above the Néel temperature. In particular, we used simply stacked single and triple layered clusters, which are non-bipartite in the direction of the weak hopping t'. Tables listing the clusters are given in Appendix B.

The impurity solver employed in the study is the continuous time auxiliary field quantum Monte Carlo solver [37] with sub-matrix updates [38].

2.1 Framework for multisite unit cells

In this subsection we present the notation for description of a general non-Bravais lattice consisting of ℓ-site unit cells. The general translationally invariant non-interacting Hamiltonian on such a lattice is of the form

$$
\hat{H}^0 = - \sum_{\mathbf{r}, \mathbf{r}', \alpha, \alpha', \sigma} \tilde{t}_{(\mathbf{r}' - \mathbf{r}) \alpha \alpha'} \hat{c}_{\mathbf{r}\alpha\sigma}^\dagger \hat{c}_{\mathbf{r}'\alpha'\sigma}. \tag{2}
$$

The site position is described by a pair of cell realspace position $\mathbf{r}$ ($\mathbf{r}'$) and of an sublattice index α (α'). The cell realspace position is an integer linear combination of the lattice basis vectors $\mathbf{a}_i$, the sublattice index is a number from $\{1, 2, \ldots, \ell\}$, and $\sigma \in \{\uparrow, \downarrow\}$.

We use a Fourier transformation (FT) to relate creation operators in reciprocal space and real space,

$$\hat{c}^{\dagger}_{\mathbf{r}\alpha\sigma} = \frac{1}{\sqrt{L}} \sum_{\mathbf{k}} e^{-i\mathbf{k}\cdot(\mathbf{r}+\mathbf{r}_{\alpha})} \hat{c}^{\dagger}_{\mathbf{k}\alpha\sigma}, \quad (3)$$

where $\mathbf{r}_{\alpha}$ is the intracell position vector of site α, and L is the number of unit cells.

The Green's function can be conveniently given in a matrix form,

$$[G_{\sigma}(\mathbf{k}, i\omega_n)]_{\alpha\alpha'} \equiv -\int_0^{\beta} d\tau \, e^{i\omega_n\tau} \left\langle \hat{c}_{\mathbf{k}\alpha\sigma}(\tau)\hat{c}^{\dagger}_{\mathbf{k}\alpha'\sigma} \right\rangle. \quad (4)$$

The explicit form of the non-interacting lattice Green's function in Matsubara representation in reciprocal space is as follows,

$$\left[G^0_{\sigma}(\mathbf{k}, i\omega_n)\right]_{\alpha\alpha'} = \left[\left(i\omega_n \mathbb{1}_{\ell} + \tilde{T}_{\mathbf{k}}\right)^{-1}\right]_{\alpha\alpha'}, \quad (5)$$

where $\tilde{T}_{\mathbf{k}}$ is an $\ell \times \ell$ matrix composed of the Fourier transformed $\tilde{t}_{\boldsymbol{\Delta}\alpha\alpha'}$,

$$\left(\tilde{T}_{\mathbf{k}}\right)_{\alpha\alpha'} = \tilde{t}_{\mathbf{k}\alpha\alpha'} = e^{i\mathbf{k}\cdot(\mathbf{r}_{\alpha'}-\mathbf{r}_{\alpha})} \sum_{\boldsymbol{\Delta}} e^{i\mathbf{k}\cdot\boldsymbol{\Delta}} \, \tilde{t}_{\boldsymbol{\Delta}\alpha\alpha'}. \quad (6)$$

For the self energy, which is defined by the Dyson equation, we use the same matrix notation as for the Green's functions.

2.2 DCA method for multisite unit cells

We employ a generalization of the DCA method applicable for translationally invariant models with unit cells containing ℓ sites, introduced in studies of the (extended) Hubbard model on the honeycomb lattice [39,40] and to allow study of symmetry broken phases in a two-dimensional Kondo lattice model [41].

A cluster is a parallelepiped defined by cluster basis vectors $\tilde{\mathbf{a}}_i \equiv \sum_{j=1}^{3} c_{ij}\mathbf{a}_j$ with integer c_{ij}. The cluster defines a superlattice of which it is the unit cell. The Brillouin zone of the superlattice is the DCA patch around the $\Gamma = \mathbf{0}$ point. In order to make the patch compact in terms of dispersion variations, we choose it to be the Wigner-Seitz cell constructed with distance function $\|\mathbf{k}\|^2 = (k_x^2 + k_y^2) + (t'/t)^2 k_z^2$, taking into account the anisotropy. Numerically it was obtained by Qhull [42].

Vectors $\mathbf{K}$ of the cluster reciprocal representation are shortly referred to as cluster reciprocal vectors. DCA approximates the lattice self energy by a patch-wise constant function. Each of the patches is the DCA patch translated by a $\mathbf{K}$ vector. The value of the lattice self energy in a patch is set equal to the cluster self energy Σ at the $\mathbf{K}$ vector in the patch center. The mapping of the lattice onto a cluster is in the reciprocal space expressed as patch averaging,

$$G(\mathbf{K}) = \frac{1}{\Omega} \int_{\text{patch}} d\tilde{\mathbf{k}} \underbrace{\left[G^0(\mathbf{K}+\tilde{\mathbf{k}})^{-1} - \Sigma(\mathbf{K})\right]^{-1}}_{G^{\text{lat}}(\mathbf{K}+\tilde{\mathbf{k}})}, \quad (7)$$

where $G^{\text{lat}}(\mathbf{k})$ is the DCA approximation of the interacting lattice Green's function. equation (7) implicitly defines the interacting cluster Green's function $G(\mathbf{K})$ and $\Sigma(\mathbf{K})$. For shortness we suppressed the Matsubara frequencies $i\omega_n$ and spin projection σ in all quantities. Ω denotes the patch volume. Notice that the mapping condition is formally identical to the DCA mapping for Bravais lattices, with corresponding quantities being $\ell \times \ell$ matrices instead of scalars.

The mapping in equation (7) is solved iteratively starting with a guess of the non-interacting cluster Green's function $\mathscr{G}^0(\mathbf{K})$ provided as in input to the impurity solver computing $G(\mathbf{K})$. The cluster self energy is then obtained via Dyson equation

$$\Sigma(\mathbf{K}) = \mathscr{G}^0(\mathbf{K})^{-1} - G(\mathbf{K})^{-1}. \quad (8)$$

Performing the patch averaging

$$\bar{G}^{\text{lat}}(\mathbf{K}) = \frac{1}{\Omega} \int_{\text{patch}} d\tilde{\mathbf{k}} \left[G^0(\mathbf{K}+\tilde{\mathbf{k}})^{-1} - \Sigma(\mathbf{K})\right]^{-1}, \quad (9)$$

and once again using the Dyson equation,

$$\mathscr{G}^0(\mathbf{K}) = \left[\bar{G}^{\text{lat}}(\mathbf{K})^{-1} + \Sigma(\mathbf{K})\right]^{-1}, \quad (10)$$

one obtains next guess of $\mathscr{G}^0(\mathbf{K})$. The convergence is reached when $G(\mathbf{K}) = \bar{G}^{\text{lat}}(\mathbf{K})$, which exactly is the mapping condition in equation (7).

Note that the averaging step of equation (9) makes the DCA with multisite cells sensitive to the specific choice of FT. Omitting the phase factors $e^{-i\mathbf{k}\cdot\mathbf{r}_{\alpha}}$ in equation (3) in the FT, as done in reference [41], leads, in general, to different results for any finite size cluster[1]. For a Bravais lattice it can be shown that the DCA with enabled (spontaneous) translational symmetry breaking [33] is equivalent to our version with enlarged unit cell if the FT has the form given in equation (3). Moreover, the choice of FT produces a slower varying $G^0(\mathbf{k})$ within a patch, thus effectively reducing the mean-field effects associated with the averaging[2]. The difference originates from the slower varying off-diagonal elements of $\tilde{T}_{\mathbf{k}}$. Another advantage of the FT form shows up if the problem possesses point group symmetries, as these then directly propagate to the Green's functions.

3 Results

We compute the EOS and further properties – the energy, entropy, density, nearest-neighbor spin correlation, and the double occupancy – of the model of equation (1) by using DCA and extrapolating to the thermodynamic

---

[1] The difference, if present, vanishes for $L \to \infty$, as the integral in equation (9) becomes trivial and the method is exact.

[2] The asymptotic behavior with number of unit cells L of the cluster is not affected by the choice of the FT. However, the minimal cluster size needed for a reliable extrapolation may differ.

limit according to $L^{-2/3}$ (see Refs. [34,43] for details). We restrict the calculations to fillings $n \leq 1$ per site, as the results for $1 < n \leq 2$ are related to those for $n \leq 1$ via particle-hole symmetry.

3.1 Free energy and entropy

The entropy per site s is estimated by numeric integration at fixed U and μ, starting from a high temperature $T_u/t = 50$,

$$s(T) = s(T_u) + \frac{f(T)}{T} - \frac{f(T_u)}{T_u} + \int_T^{T_u} \frac{f(T') \, dT'}{T'^2}. \quad (11)$$

Here, $f(T) = e(T) - \mu n(T)$, with e the energy per site and n the density per site. The value of $s(T_u)$ is obtained from a high-temperature series expansion,

$$s(T_u) = \ln 4 - \frac{1}{2T_u^2}\left[\frac{U^2}{16} + \frac{(\mu - U/2)^2}{2} + \frac{Z_t t^2 + 2t'^2}{2}\right]$$
$$+ \frac{U(\mu - U/2)^2}{8T_u^3} + O(T_u^{-4}). \quad (12)$$

The expression for $e(T)$ is explicitly given in equation (C.1). We provide the EOS at half filling for interactions $U/t = 1, 2, 3, 4, 6, 8$ and anisotropies $t/t' = 1, 2, 4, 8$ for both stacked honeycomb and stacked square lattice. For the stacked honeycomb lattice we choose two parameter sets $(U/t, t/t') = (6, 6)$ and $(4, 4)$, at which we obtain the EOS at a wide range of fillings. For the stacked square lattice we do the same at $(U/t, t'/t) = (6, 6)$. The EOS, being one of the main outcomes of the study, is presented in the Supplemental Material[3]. Since the experiments are performed at approximatively constant total entropy, the knowledge of the entropy dependence on the density, temperature, and model parameters is essential for any experiment-theory comparison. By fitting of the density in a trapped system it is possible to infer its temperature [44].
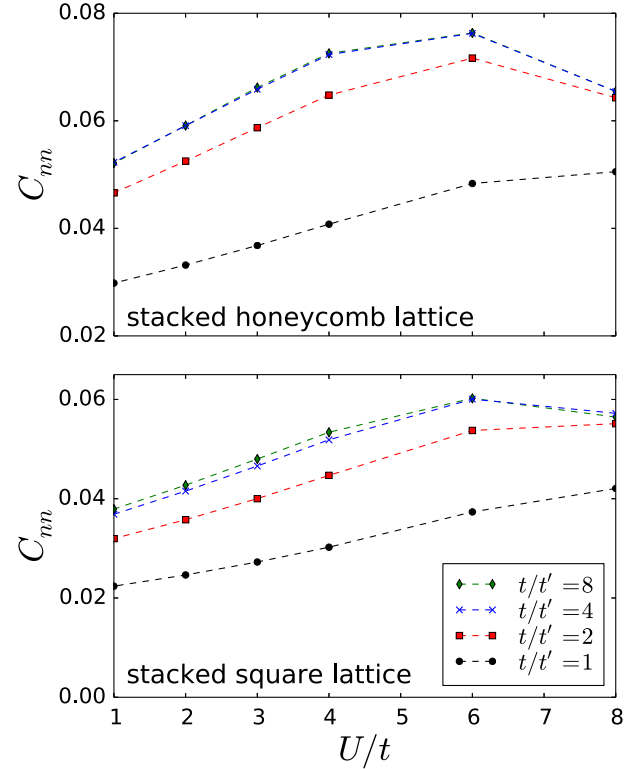
3.2 Spin correlations

We calculated the nearest-neighbor spin correlations [22], which capture the onset of magnetic ordering and have proven to be a suitable observable for estimate of the temperature of the system [23,34]. We specifically calculate the equal-time in-plane nearest-neighbor spin correlations

$$C_{nn} = -\frac{2}{Z_t L \ell} \sum_{\langle i,j \rangle} \left\langle \hat{S}_i^z \hat{S}_j^z \right\rangle, \quad (13)$$

where the sum runs over in-plane nearest-neighbor pairs (coupled by the strong hopping t), $\hat{S}_i^z = \frac{1}{2}(\hat{n}_{i\uparrow} - \hat{n}_{i\downarrow})$, L is the number of cells, and the average $\left\langle \hat{S}_i^z \hat{S}_j^z \right\rangle$ is measured

---

[3] The EOS accompanied by a python script for LDA is provided as Supplemental Material⋆.


Fig. 2. The nearest neighbor in-plane spin correlation C_{nn} for the stacked honeycomb lattice (top) and stacked square lattice (bottom) as a function of the interaction strength U/t for various anisotropies t'/t at half filling ($n = 1$, $\mu = U/2$) and at an entropy $s = 0.7$. C_{nn} shows an enhancement in the anisotropic case $t/t' > 1$. The curves for $t/t' = 4$ and 8 are on top of each other.

directly on the cluster. We show the spin correlations for the stacked honeycomb and stacked square lattice in Figure 2. The data shown was calculated for a homogeneous system at half filling and at a fixed entropy per particle. C_{nn} shows similar behavior with interaction strength and anisotropy for both lattices, with an approximative amplification by a factor $4/3$ in the stacked honeycomb lattice. The factor $4/3$ is the ratio of strong hopping coordination numbers Z_t on the stacked square lattice to that of the stacked honeycomb lattice. The maxima are at similar interaction strengths if interactions are measured in units of the bandwidth W. Qualitatively, the observed behavior is captured by the second order high-temperature expansion, which is (at half filling) given by

$$C_{nn}^{(2)}(s) = \frac{2(\ln 4 - s)t^2}{8(Z_t t^2 + 2t'^2) + U^2}. \quad (14)$$

Quantitatively, the second order high-temperature estimate of $C_{nn}(T)$ is reliable only for $T/t \gtrsim 3$, corresponding to an entropy per site s well above 1. Note that Figure 2 is calculated for $s = 0.7$, which is close the lowest experimentally realizable value at half filling [23]. Noticeably, the sum of $C_{nn}^{(2)}(s)$ over all bonds $\langle i, j \rangle$ is independent of the lattice properties if U is scaled according to the root
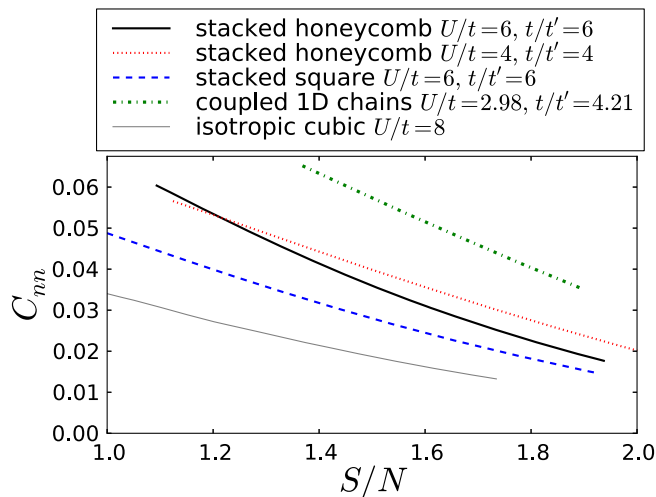
Fig. 3. Average spin correlation C_{nn} per particle plotted as a function of the entropy per particle S/N in a quadratic trap with chemical potential adjusted to obtain half filling ($n = 1$) in the trap center. The data for the coupled 1D chains and isotropic cubic lattice is taken from references [23,34].

of the second moment of the non-interacting density of states $D_2 = Z_t t^2 + 2t'^2$.

C_{nn}, as an experimentally measurable quantity [22], may serve as a sensitive thermometer in the temperature range $T/t \sim 1$ if compared with the EOS we provide. The enhancement due to anisotropy raises the signal and renders the measurement more precise.

3.3 Trap effects

In experiments, ultracold atoms are confined by a trapping potential, which may be modeled by a local density approximation (LDA) at currently experimentally accessible temperatures [45,46]. As confining potential we take a quadratic function $V(\mathbf{x})$ with minimum in the trap center. The chemical potential μ we choose such that the system is half-filled in the trap center. Assuming a large lattice, we use a continuous approximation instead of discrete summation over lattice sites and obtain a trap-averaged quantity Q as:

$$Q = \int d^3\mathbf{x} \, q \left(\mu - V(\mathbf{x}); T\right), \tag{15}$$

where q is the density of the quantity of interest in a homogeneous system. With this definition, the quantity Q per particle, Q/N, is independent on the specific parameters of the quadratic potential. For the LDA calculations we need the EOS at low filling, which we approximate by the EOS of the corresponding non-interacting system. Figure 3 shows the trap-averaged C_{nn}. Even in the trap, with contribution from sites at all fillings, the C_{nn} is at fixed entropy per site roughly proportional to Z_t^{-1}. This observation may be confronted with the experimental results presented in Figure 2a in [24], where Greif et al.
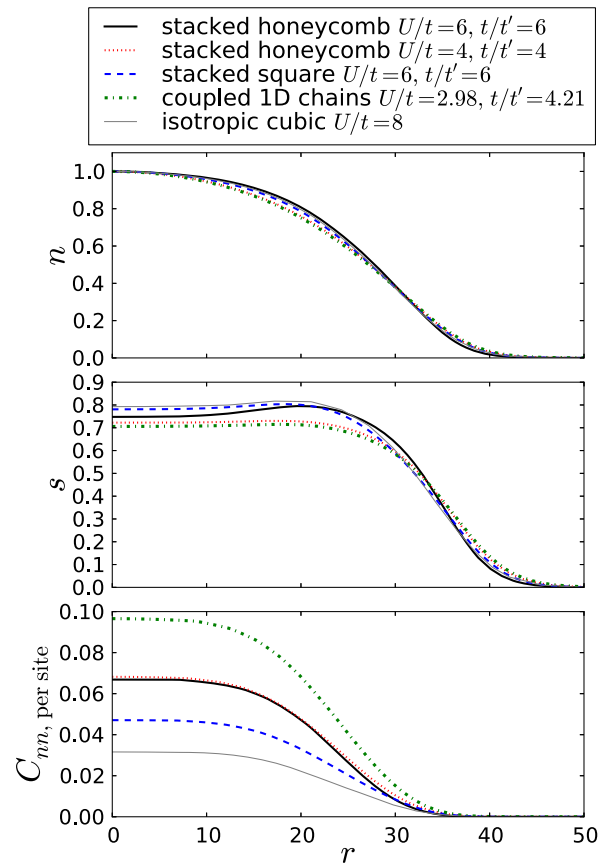
Fig. 4. Density n, entropy s, and C_{nn} profile in a quadratic trap with the particle number fixed to $N = 10^5$ and half filling in its center. The radius r is given in units of lattice sites. The entropy per particle S/N is set to 1.4, which is an experimentally achievable value [23]. The data for the coupled 1D chains and isotropic cubic lattice is taken from references [23,34].

present the trap-averaged nearest-neighbor spin correlations obtained in weakly coupled square stacks with varying ratio of in-plane hoppings. In particular, they find for $Z_t = 2$ almost doubled spin correlations when compared to $Z_t = 4$, which is consistent with our outcome. Their measurement is conducted after a nearly adiabatic ramp of the optical lattice, in a system with total entropy not significantly dependent on the chosen ratio of in-plane hoppings. In Figure 4 we display profiles of density, entropy per site, and C_{nn} for the stacked honeycomb and square lattice and the 1D coupled chains. For Figure 4 we assume isotropic $V(\mathbf{x})$. The distance from the trap center we denote by r. In the studied temperature regime, coupled 1D chains [23] show the largest spin correlation[4]. The density and entropy distributions differ only marginally. Therefore, a dynamic change of topology of the lattice, as done in reference [24], is not accompanied by a substantial particle redistribution, which may lead to unwanted

---

[4] For the 1D chain the C_{nn} is the nearest-neighbor spin correlation in direction of the strong hopping, see definition in reference [23].

heating [47]. In the lower panel of Figure 4 we observe that C_{nn} at half filling ($r = 0$) is roughly proportional to the inverse strong hopping coordination number Z_t^{-1}. This effect might be qualitatively explained by the different energy scales of the hoppings – the simulations are performed at a high temperature relative to the weak hopping t', but the temperature is comparable with the strong hopping t. Thus the antiferromagnetic short-range correlations tend to build up in the strong hopping directions (in-plane) and the singlet formation is facilitated by lower Z_t.

3.4 Double occupancy and adiabatic cooling

Of further experimental interest are ways to cool the particles, to provide access to interesting low temperature phenomena. As discovered in reference [48], an analogue of the Pomeranchuk effect can be used to cool fermions in an optical lattice. These lower their temperature T in an adiabatic process of (slow) increase of the interaction strength if the double occupancy $D = \frac{1}{L\ell}\langle n_{i\uparrow}n_{i\downarrow}\rangle$ shows an increase upon cooling at fixed density n. The adiabatic cooling effect $(\frac{\partial T}{\partial U})_{s,n}$ is proportional to the temperature, to the inverse of the specific heat, and to $(\frac{\partial D}{\partial T})_{U,n}$ [48]. The interaction driven adiabatic cooling was experimentally utilized for a $SU(6)$ Hubbard model [49]. For the Hubbard model in the context of optical lattice experiments, the presence of the effect was numerically observed both for square and honeycomb lattices [29,50].

We here investigate this effect for the stacked lattices in a homogeneous system. Figure 5 shows the adiabatic cooling effect at half filling and at entropy per site $s = 0.7$ at a range of anisotropies, with cooling persisting up to $U/t \approx 6$. Alternatively it is possible to start from large interactions and decrease U; however, in that case T/U may increase. The cooling is present only at sufficiently low entropies, $s \lesssim 0.8$, and it is accompanied by an approximate maximization of C_{nn} according to Figure 2 (top). The stacked square lattice shows the largest effect in its isotropic limit, which is the cubic lattice.

Figure 6 shows $(\frac{\partial D}{\partial T})_{U,n}$ away from half filling. Cooling here appears at even higher temperature than in the half filled case. This might be utilized to transfer entropy from the region with half filling to less densely occupied regions in the trap. While realistic cooling design was discussed in references [51,52], we only note that the low density regions show large entropy per particle and thus they may store a large portion of the total entropy. Figure 6 shows that there are no qualitative but only subtle quantitative differences in between the examined lattices with respect to the presence and strength of the cooling phenomenon. As the magnitude of $(\frac{\partial D}{\partial T})_{U,n}$ does not show great differences among the investigated lattices, the cooling effect is of comparable strength with some enhancement in the case of stacked honeycomb lattice at density near to the half filling.
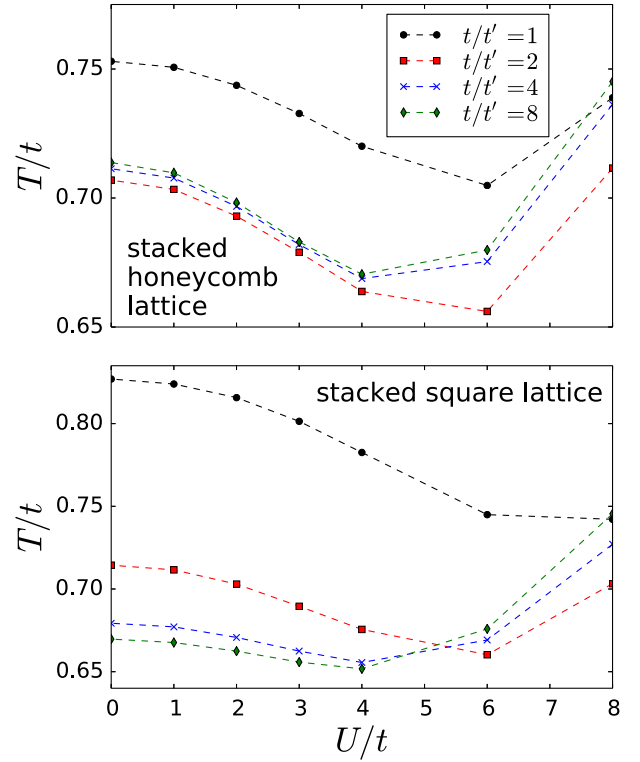
Fig. 5. Temperature T/t plotted as a function of U/t for the stacked honeycomb (top) and stacked square lattice (bottom) at half filling and at entropy per site $s = 0.7$ for various anisotropies t/t'. An adiabatic increase of U/t from 0 up to a parameter-specific U induces cooling in all cases.

3.5 Néel transition

The entropy per particle at the Néel temperature T_N is expected to decrease for large anisotropies, in accordance with the Mermin-Wagner-Hohenberg theorem [31,32]. We investigate the Néel transition for half filling only. In order to identify the lattice with the largest entropy per site at the Néel transition, s_N, we therefore focused on smaller anisotropies in this part. Since any mean-field theory overestimates ordering, the T_N and s_N for a specific cluster provides an upper bound of the corresponding quantities in the thermodynamic limit. For an unbiased estimate we localize the transition temperature for several clusters and extrapolate the transition temperature T_N as suggested in reference [53], using the critical exponent $\nu = 0.71$ for the 3D Heisenberg model [54]. For the stacked square lattice of anisotropy $t/t' = 4$ we managed to obtain the T_N estimate for a cluster with 384 sites. We checked that disregarding data for this largest cluster in the extrapolation, keeping data for clusters only up to 100 sites, changes T_N by about the error estimate. Example of the T_N extrapolation is provided in Figure A.1. The entropy s_N is obtained as $s(T_N)$. To its error estimate contribute both uncertainty of T_N and error of the numerical integration of s. T_N and s_N calculated for the different systems studied in this paper are summarized in Table 1.
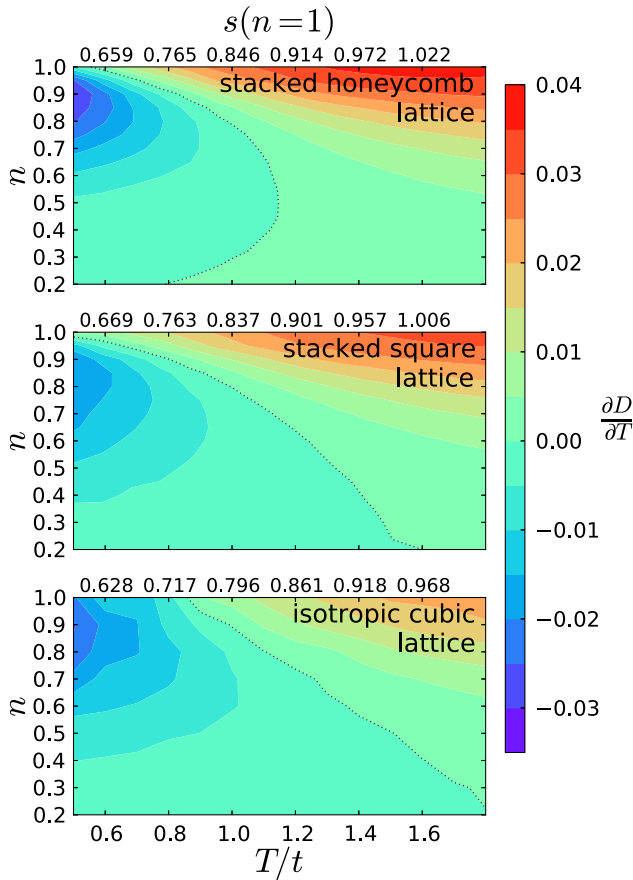
Fig. 6. Negative values of $\left(\frac{\partial D}{\partial T}\right)_{U,n}$ indicate presence of the effect of adiabatic cooling upon interaction increase. The corresponding quantity is plotted as a function of T and n for the stacked honeycomb (top) and stacked square lattice (middle) at $U/t = 6$ and $t/t' = 6$. For comparison we show the same quantity for isotropic cubic lattice at $U/t = 6$ in the bottom panel, using data from reference [34]. The regions of positive and negative $\frac{\partial D}{\partial T}$ are separated by dotted line. For a fair comparison we add upper axis with entropy per site of half filled system, $s(n = 1)$, at temperature given by the temperature axis common to all plots.

4 Conclusion

For both lattice structures we calculated the EOS at half filling for anisotropies $1 \leq t/t' \leq 8$ and interactions $1 \leq U/t \leq 8$, and for a few parameter sets we obtained the EOS for a wide range of fillings. The EOS data is provided in the Supplemental Material[3]. It allows for LDA based trap-specific calculations, suitable for calibration and optimization of ultracold atoms experiments. In particular it may be used for estimating the amount of heating during the lattice loading and for estimating the temperature and entropy, if the experiment provides a temperature sensitive measurement and the value of the initial entropy [23].

For stacked lattices we found enhanced short-range in-plane correlations for experimentally accessible temperatures of the order t. We investigated the possibility of interaction-driven adiabatic cooling, which is present in the studied systems and may contribute to the progress

Table 1. Néel temperatures and entropies for both examined stacked lattices. For stacked square lattice we studied wide range of anisotropies as those may be of interest with respect to undoped high-T_c superconductor parent materials. Missing s_N entries indicate that we did not integrate the entropy down to T_N. The isotropic cubic lattice data for $U/t = 4, 8$ is from reference [23].

		Stacked square		Stacked honeycomb	
t/t'	U/t	T_N/t	s_N	T_N/t	s_N
	4	0.1955(25)	0.223(18)	0.206(1)	
1	6	0.324(2)	0.430(8)	0.292(4)	0.405(35)
	8	0.3595(83)	0.487(23)	0.299(2)	0.33(10)
	4	0.206(2)	0.313(49)	0.173(4)	
2	6	0.293(4)	0.438(39)	0.239(11)	0.28(8)
	8	0.294(8)	0.41(6)	0.205(21)	
	4	0.200(2)	0.30(7)		
4	6	0.245(7)	0.28(11)		
	8	0.219(8)			
8	4	0.185(2)			
	6	0.208(7)			

in cooling ultracold atoms. We computed the Néel temperature for both investigated stacked lattices. Among them, the lattice with highest critical entropy per particle at half filling is the conventional isotropic cubic lattice with interaction $U/t \approx 8$. For stacked square lattice we investigated the Néel temperature also for larger anisotropies, up to $t/t' = 8$, as the stacked square lattice at half filling is an effective model for the undoped high-T_c superconductors.

Author contribution statement

The simulations were run and post-processed by J. Imriška, the program was developed by E. Gull and J. Imriška. All authors contributed to writing the paper.

Appendix A: Susceptibility measurement

This section provides details on the susceptibility measurement in the DCA with ℓ-site cell. It is a generalization of the susceptibility measurement described in reference [33]. We stick to the naming and denotations used therein.

Our interest is in the static (zero bosonic frequency ν) susceptibility corresponding to the staggered magnetization operator,

$$\hat{m} = \frac{1}{L\ell} \sum_{\mathbf{r},\alpha,\sigma} e^{i\mathbf{Q}\cdot\mathbf{r}} f_\alpha \, \sigma \, \hat{n}_{\mathbf{r}\alpha\sigma}, \qquad (A.1)$$

with $\sigma = \pm 1$. For the stacked square lattice we use a description with a single site per unit cell and $\mathbf{Q}$ is then the antiferromagnetic reciprocal vector (π,π,π), and $f_A = 1$. For the stacked honeycomb lattice we performed simulations in the paramagnetic regime with 2-site unit cell depicted in Figure 1 (left) and we measured the susceptibility at $\mathbf{Q} = (0,0,\pi)$; with sublattice factors $f_A = 1$, $f_B = -1$.

In the following we assume $\mathbf{Q} \neq \mathbf{0}$ to simplify the formulas, as both cases satisfies that condition. We assume the $\mathbf{Q}$ vector to be contained in the set of cluster reciprocal vectors.

We follow these steps:

1. The two-particle cluster Green's function $\chi_c(\mathbf{Q}, i\nu)$ is measured using the CTAUX impurity solver [37] and Wick's theorem.
2. The irreducible cluster vertex $\Gamma_c(\mathbf{Q}, i\nu)$ is then obtained via Bethe–Salpeter equation,

$$\Gamma_c(\mathbf{Q}, i\nu) = \chi_c^0(\mathbf{Q}, i\nu)^{-1} - \chi_c(\mathbf{Q}, i\nu)^{-1}. \qquad (A.2)$$

3. We approximate the irreducible lattice vertex $\Gamma(\mathbf{Q}, i\nu)$ by the cluster vertex $\Gamma_c(\mathbf{Q}, i\nu)$. $\Gamma(\mathbf{Q}, i\nu)$ will thus be patch-wise constant in reciprocal space.
4. The lattice two-particle cluster Green's function $\chi(\mathbf{Q}, i\nu)$ is obtained via Bethe–Salpeter equation.

$$\chi(\mathbf{Q}, i\nu)^{-1} = \chi^0(\mathbf{Q}, i\nu)^{-1} - \Gamma(\mathbf{Q}, i\nu). \qquad (A.3)$$

Since the vertex Γ is patch-wise constant, we may perform patch averaging to obtain

$$\bar{\chi}(\mathbf{Q}, i\nu)^{-1} = \bar{\chi}^0(\mathbf{Q}, i\nu)^{-1} - \Gamma(\mathbf{Q}, i\nu). \qquad (A.4)$$

5. The lattice susceptibility is computed from $\bar{\chi}(\mathbf{Q}, i\nu)$.

The precise definitions of all quantities are given below.

For the matrices $\chi_{(c)}(\mathbf{Q}, i\nu)$, $\Gamma_{(c)}(\mathbf{Q}, i\nu)$, and $\chi_{(c)}^0(\mathbf{Q}, i\nu)$ we use multiindex notation $K \equiv (\mathbf{K}\alpha\gamma n\sigma)$, where $\mathbf{K}$ is a cluster reciprocal vector, α and γ are intracell site labels, n is the index of the Matsubara frequency ω_n, and σ is the spin projection. The KK' element of the two-particle cluster Green's function $\chi_c(\mathbf{Q}, 0)$ is defined by:

$$\frac{1}{\beta} \int_0^\beta \int_0^\beta \int_0^\beta \int_0^\beta d\tau_1 \, d\tau_2 \, d\tau_3 \, d\tau_4$$
$$\times \, e^{-i(\omega_n \tau_1 - \omega_n \tau_2 + \omega_{n'} \tau_3 - \omega_{n'} \tau_4)}$$
$$\times \left\langle T_\tau c^\dagger_{\mathbf{K}+\mathbf{Q}\alpha\sigma}(\tau_1) c_{\mathbf{K}\gamma\sigma}(\tau_2) c^\dagger_{\mathbf{K}'\alpha'\sigma'}(\tau_3) c_{\mathbf{K}'+\mathbf{Q}\gamma'\sigma'}(\tau_4) \right\rangle. \qquad (A.5)$$

The noninteracting cluster susceptibility χ_c^0 and its patch-averaged lattice counterpart $\bar{\chi}^0$ are defined by:

$$\left[\chi_c^0(\mathbf{Q}, 0)\right]_{KK'} = -\beta \delta_{\sigma\sigma'} \delta_{nn'} \delta_{\mathbf{K}\mathbf{K}'} \left[G(\mathbf{K}, i\omega_n)\right]_{\alpha\gamma'}$$
$$\times \left[G(\mathbf{K}+\mathbf{Q}, i\omega_n)\right]_{\alpha'\gamma}, \qquad (A.6)$$

$$\left[\bar{\chi}^0(\mathbf{Q}, 0)\right]_{KK'} = -\frac{\beta \delta_{\sigma\sigma'} \delta_{nn'} \delta_{\mathbf{K}\mathbf{K}'}}{\Omega}$$
$$\times \int_{\text{patch}} d\tilde{\mathbf{k}} \left[G^{\text{lat}}(\mathbf{K}+\tilde{\mathbf{k}}, i\omega_n)\right]_{\alpha\gamma'}$$
$$\times \left[G^{\text{lat}}(\mathbf{K}+\mathbf{Q}+\tilde{\mathbf{k}}, i\omega_n)\right]_{\alpha'\gamma}, \qquad (A.7)$$

with cluster (lattice) Green's function G (G^{lat}), and Kronecker delta δ_{ij}.

The static staggered spin susceptibility of the lattice may be obtained by:

$$\chi_{AF} = \frac{1}{L\ell\beta^2} \sum_{\sigma,\sigma'} \sigma\sigma' \sum_{\alpha,\alpha'} f_\alpha f_{\alpha'} \sum_{\mathbf{K},\mathbf{K}'} e^{i\mathbf{Q}'\cdot\mathbf{r}_\alpha} e^{i\mathbf{Q}''\cdot\mathbf{r}_{\alpha'}}$$
$$\times \sum_{n,n'} \bar{\chi}_{\mathbf{K}\alpha\alpha n\sigma \mathbf{K}'\alpha'\alpha'n'\sigma'}(\mathbf{Q}, i\nu = 0), \qquad (A.8)$$

with patch-averaged two-particle lattice Green's function $\bar{\chi}$ at the reciprocal vector $\mathbf{Q}$ and at zero frequency ν; and with intracell phase factors,

$$e^{i\mathbf{Q}'\cdot\mathbf{r}_\alpha} \equiv e^{-iK_{\text{repr}}(\mathbf{K}+\mathbf{Q})\cdot\mathbf{r}_\alpha} e^{iK_{\text{repr}}(\mathbf{K})\cdot\mathbf{r}_\alpha},$$
$$e^{i\mathbf{Q}''\cdot\mathbf{r}_{\alpha'}} \equiv e^{-iK_{\text{repr}}(\mathbf{K}')\cdot\mathbf{r}_{\alpha'}} e^{iK_{\text{repr}}(\mathbf{K}'+\mathbf{Q})\cdot\mathbf{r}_{\alpha'}}, \qquad (A.9)$$

where $K_{\text{repr}}(\mathbf{K})$ is the representative of the cluster reciprocal vector $\mathbf{K}$ used in the simulation, which may differ from $\mathbf{K}$ by a reciprocal lattice vector[5].

The frequencies ω_n, $\omega_{n'}$ need for any practical use be cut-off at some ω_c. The frequency cut-off is cured by fitting the $\frac{1}{\omega_n^2}$ tail and adding its contribution to the result [57]. The cut-off was validated by comparison of the extrapolated impurity susceptibility, obtained by equation (A.8) with $\bar{\chi}$ replaced by χ_c, with the directly measured cluster susceptibility,

$$\chi_{AF,c} = L\ell \int_0^\beta d\tau \, \langle \hat{m}(\tau)\hat{m} \rangle, \qquad (A.10)$$

with $\hat{m}$ given in equation (A.1). Typically we used $\omega_c \approx 5U$.

The DCA, as a mean field based method, displays close to the second order phase transition the mean field critical exponents. We utilize that for a precise location of the transition for each cluster by searching for the intersection of $\chi_{AF}^{-\gamma_{\text{mf}}}$ with zero, with the mean field critical exponent $\gamma_{\text{mf}} = 1$.

A comparison of the susceptibility based results measured in the paramagnetic (PM) regime with the results

---

[5] The Green's function shifted by a reciprocal vector $\mathbf{G}$ is given by $G(\mathbf{k}+\mathbf{G}) = U_\mathbf{G}^+ G(\mathbf{k}) U_\mathbf{G}$ with diagonal unitary matrix $(U_\mathbf{G})_{\alpha\alpha'} = \delta_{\alpha\alpha'} e^{i\mathbf{G}\cdot\mathbf{r}_\alpha}$.
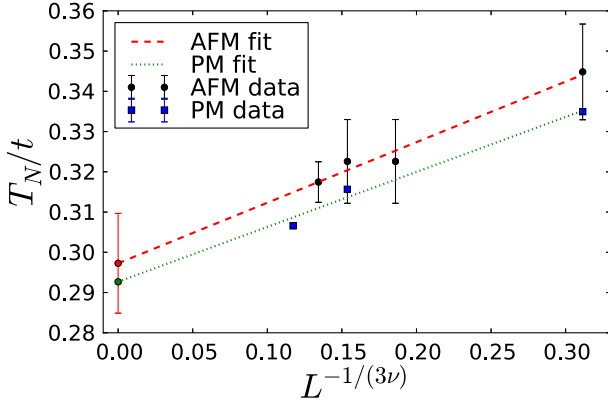
Fig. A.1. Extrapolation of the T_N for the stacked honeycomb for $t/t' = 1$, $U/t = 6$. The critical exponent $\nu = 0.71$ was chosen as that of the the 3D Heisenberg model. The error bars for the AFM data show lower and upper bounds of the transition based on measurement of the staggered magnetization. The PM data points are susceptibility based measurement with error bars smaller than the symbol size.

Table B.1. Clusters used for the EOS calculations on the stacked square lattice. For $T/t > 4$ we used only the two smallest clusters.

t/t'	L	Cluster basis
1	36	$(1, 0, 3), (3, 2, -1), (2, -2, -2)$
	56	$(1, 2, 3), (-2, 3, -1), (-4, -1, 1)$
	64	$(1, 2, 3), (-2, 4, 2), (-1, -2, 5)$
	74	$(1, 3, 4), (3, 4, -1), (-2, 2, -2)$
2	8	$(0, 0, 1), (2, 2, 0), (-2, 2, 0)$
	36	$(0, 0, 2), (3, 3, 0), (-3, 3, 0)$
	102	$(1, 0, 3), (5, 3, 0), (-3, 5, 0)$
4	8	$(0, 0, 1), (2, 2, 0), (-2, 2, 0)$
	18	$(0, 0, 1), (3, 3, 0), (0, -3, 3, 0)$
	116	$(0, 0, 2), (7, 3, 0), (-3, 7, 0)$
6	8	$(0, 0, 1), (2, 2, 0), (-2, 2, 0)$
	18	$(0, 0, 1), (3, 3, 0), (-3, 3, 0)$
	34	$(0, 0, 1), (5, 3, 0), (-3, 5, 0)$
	74	$(0, 0, 1), (7, 5, 0), (-5, 7, 0)$
8	8	$(0, 0, 1), (2, 2, 0), (-2, 2, 0)$
	18	$(0, 0, 1), (3, 3, 0), (-3, 3, 0)$
	58	$(0, 0, 1), (7, 3, 0), (-3, 7, 0)$

obtained by direct observation of spontaneous magnetization in a formulation with doubled unit cell (with 4 sites per cell) allowing for antiferromagnetic (AF) ordering are displayed in Figure A.1. The extrapolation is done both with equally weighted $T_N(L)$, as well as with weights inversely proportional to the square of the error estimate of $T_N(L)$.

Appendix B: Clusters used in the simulations

A complete list of clusters used for the EOS calculations is provided in Tables B.1–B.5, given in terms of the integer components c_{ij} as (c_{i1}, c_{i2}, c_{i3}) for $i = 1, 2, 3$. In order to lower potential bias by the choice of the cluster geometry,

Table B.2. Clusters used for the stacked honeycomb lattice to obtain the EOS at half filling.

t/t'	L	Temperature	Cluster basis
1	6	$T/t > 0.6$	$(2, -1, 0), (-1, 2, 0), (0, 0, 2)$
	18		$(2, 2, 0), (0, 3, 0), (0, 0, 3)$
	27		$(3, 0, 0), (0, 3, 0), (0, 0, 3)$
	36	$T/t < 4$	$(3, 0, 0), (0, 3, 0), (0, 0, 4)$
	48	$T/t < 4$	$(4, -2, 0), (-2, 4, 0), (0, 0, 4)$
2	3		$(2, -1, 0), (-1, 2, 0), (0, 0, 1)$
	18		$(3, 0, 0), (0, 3, 0), (0, 0, 2)$
	54	$T/t < 4$	$(4, 1, 0), (-2, 4, 0), (0, 0, 3)$
4	3	$T/t > 4$	$(2, -1, 0), (-1, 2, 0), (0, 0, 1)$
	9		$(3, 0, 0), (0, 3, 0), (0, 0, 1)$
	66		$(8, -1, 0), (1, 4, 0), (0, 0, 2)$
8	9		$(3, 0, 0), (0, 3, 0), (0, 0, 1)$
	21		$(5, -4, 0), (-1, 5, 0), (0, 0, 1)$
	39	$T/t < 4$	$(7, -5, 0), (-2, 7, 0), (0, 0, 1)$

Table B.3. Clusters used to obtain the EOS at $(U/t, t/t') = (6, 6)$ and $(4, 4)$ for the stacked honeycomb lattice. *The 39-cell cluster was not used in case of $(U/t, t/t') = (4, 4)$ for $\mu/t < -2$, in which case three clusters only were used.

L	Temperature	Cluster basis
3	$T/t > 4$	$(2, -1, 0), (-1, 2, 0), (0, 0, 1)$
9		$(3, 0, 0), (0, 3, 0), (0, 0, 1)$
12	$T/t \leq 4$	$(4, -2, 0), (-2, 4, 0), (0, 0, 1)$
21	$T/t \leq 4$	$(5, -4, 0), (-1, 5, 0), (0, 0, 1)$
39	$T/t \leq 1.5$ *	$(7, -5, 0), (-2, 7, 0), (0, 0, 1)$

Table B.4. Bipartite clusters of stacked square lattice used for the T_N estimate. For $t/t' = 2, 4$ we used two different double layered clusters of same size to minimize potential bias due to cluster choice, as the cluster with basis vector $(0, 0, 2)$ has every site doubly coupled to its neighbor in the vertical direction due to the periodic boundary conditions.

t/t'	L	Cluster basis
1	36, 56, 64, 74	same as in Table B.1 for $t = t'$
	128	$(-2, 4, 4), (2, -4, 4), (1, 6, 1)$
2	8	$(1, 0, 1), (2, 2, 0), (-2, 2, 0)$
	36	$(0, 0, 2), (3, 3, 0), (-3, 3, 0)$
	36	$(1, 1, 2), (3, 3, 0), (-3, 3, 0)$
	102	$(1, 0, 3), (5, 3, 0), (-3, 5, 0)$
4	18	$(1, 0, 1), (3, 3, 0), (-3, 3, 0)$
	100	$(0, 0, 2), (5, 5, 0), (-5, 5, 0)$
	100	$(1, 1, 2), (5, 5, 0), (-5, 5, 0)$
	384	$(1, 0, 3), (8, 8, 0), (-8, 8, 0)$
8	20	$(1, 0, 1), (4, 2, 0), (-2, 4, 0)$
	50	$(1, 0, 1), (5, 5, 0), (-5, 5, 0)$
	196	$(0, 0, 2), (7, 7, 0), (-7, 7, 0)$

in some cases we employed clusters of same size or with equal in-plane layers, but with different overall shape.

For a reliable extrapolation, the clusters need to be sufficiently large to follow the asymptotic behavior of DCA with L, assumed in the extrapolation. Non-collinear points in the extrapolation indicate insufficient cluster sizes. In general, larger clusters are needed for reliable

Table B.5. Bipartite clusters of stacked honeycomb lattice used for the T_N estimate. Similarly as for stacked square lattice we used two different 18-cell clusters to minimize potential bias by particular cluster geometry. The clusters marked with * were used only for $U = 6t$.

t/t'	L	Cluster basis
	12	$(0,0,4), (2,-1,0), (-1,2,0)$
1	54	$(0,0,6), (3,0,0), (0,3,0)$
	96	$(0,0,8), (4,-2,0), (-2,4,0)$
	18	$(0,0,2), (3,0,0), (0,3,0)$
	18	$(1,0,2), (3,0,0), (0,3,0)$
2	24^*	$(0,0,2), (4,-2,0), (-2,4,0)$
	24^*	$(1,0,2), (4,-2,0), (-2,4,0)$
	36^*	$(1,0,2), (4,-2,0), (1,4,0)$
	108	$(0,0,4), (-3,6,0), (6,-3,0)$

extrapolations at lower temperature. The numerical cost of the simulations limits the manageable sizes of the clusters, and thus the lowest accessible temperature. We checked the extrapolations for consistence within error bars with extrapolations disregarding data from smaller clusters.

Appendix C: Energy estimation and spectral moments

The energy per site e was obtained by:

$$
e = \frac{U}{L\ell} \sum_{\mathbf{r},\alpha} \langle \hat{n}_{\mathbf{r}\alpha\uparrow} \hat{n}_{\mathbf{r}\alpha\downarrow} \rangle - \frac{1}{L\ell\Omega} \sum_{\mathbf{K},\sigma} \int_{\text{patch}} d\tilde{\mathbf{k}}
$$
$$
\times \left[\mathrm{Tr}\left(T_{\mathbf{K}+\tilde{\mathbf{k}}} \right) + \frac{1}{\beta} \sum_n \mathrm{Tr}\left(T_{\mathbf{K}+\tilde{\mathbf{k}}} G_\sigma^{\text{lat}}(\mathbf{K}+\tilde{\mathbf{k}}, i\omega_n) \right) \right],
\tag{C.1}
$$

with $T_{\mathbf{k}} = \tilde{T}_{\mathbf{k}} - \mu \mathbb{1}$, $\langle \hat{n}_{\mathbf{r}\alpha\uparrow} \hat{n}_{\mathbf{r}\alpha\downarrow} \rangle$ measured directly on the cluster. The lattice Green's function $G_\sigma^{\text{lat}}(\mathbf{K}+\tilde{\mathbf{k}}, i\omega_n)$ is defined in equation (9). The high-frequency tail is added based on spectral moments given below.

The spectral moments of the full Green's function,

$$
G_\sigma(\mathbf{k}, i\omega_n) = \frac{\mathbb{1}_\ell}{i\omega_n} + \frac{C_2^{\mathbf{k}\sigma}}{(i\omega_n)^2} + \frac{C_3^{\mathbf{k}\sigma}}{(i\omega_n)^3} + O\big((i\omega_n)^{-4}\big), \tag{C.2}
$$

are used for precise FT from Matsubara representation $(i\omega_n)$ to imaginary time representation (τ). In the framework of multisite DCA in Section 2.2 they are given by expressions

$$
\left(C_2^{\mathbf{k}\sigma} \right)_{\alpha\alpha'} = -\tilde{t}_{\mathbf{k}\alpha\alpha'} + U\delta_{\alpha\alpha'} \langle n_{\alpha\bar{\sigma}} \rangle, \tag{C.3}
$$

$$
\left(C_3^{\mathbf{k}\sigma} \right)_{\alpha\alpha'} = \sum_\gamma \tilde{t}_{\mathbf{k}\alpha\gamma} \tilde{t}_{\mathbf{k}\gamma\alpha'} - \tilde{t}_{\mathbf{k}\alpha\alpha'} U \langle n_{\alpha\sigma} + n_{\alpha'\bar{\sigma}} \rangle
$$
$$
+ U^2 \delta_{\alpha\alpha'} \langle n_{\alpha\bar{\sigma}} \rangle. \tag{C.4}
$$

References

1. J. Hubbard, Proc. R. Soc. London Ser. A **276**, 238 (1963)
2. D.J. Scalapino, Does the Hubbard Model Have the Right Stuff? in *Perspectives in Many-Particle Physics* (North-Holland, 1994), pp. 95–125
3. D. Scalapino, in *Handbook of High-Temperature Superconductivity*, edited by J. Schrieffer, J. Brooks (Springer, New York, 2007), pp. 495–526
4. D. Zanchi, H.J. Schulz, Phys. Rev. B **54**, 9509 (1996)
5. S. Sorella, G.B. Martins, F. Becca, C. Gazza, L. Capriotti, A. Parola, E. Dagotto, Phys. Rev. Lett. **88**, 117002 (2002)
6. S. Raghu, S.A. Kivelson, D.J. Scalapino, Phys. Rev. B **81**, 224505 (2010)
7. T.A. Maier, M. Jarrell, T.C. Schulthess, P.R.C. Kent, J.B. White, Phys. Rev. Lett. **95**, 237001 (2005)
8. C. Huscroft, M. Jarrell, T. Maier, S. Moukouri, A.N. Tahvildarzadeh, Phys. Rev. Lett. **86**, 139 (2001)
9. B. Kyung, S.S. Kancharla, D. Sénéchal, A.M.S. Tremblay, M. Civelli, G. Kotliar, Phys. Rev. B **73**, 165114 (2006)
10. N. Lin, E. Gull, A.J. Millis, Phys. Rev. B **82**, 045104 (2010)
11. E. Gull, O. Parcollet, A.J. Millis, Phys. Rev. Lett. **110**, 216405 (2013)
12. F. Becca, S. Sorella, Phys. Rev. Lett. **86**, 3396 (2001)
13. Y. Nagaoka, Phys. Rev. **147**, 392 (1966)
14. C.C. Chang, S. Zhang, D.M. Ceperley, Phys. Rev. A **82**, 061603 (2010)
15. R. Staudt, M. Dzierzawa, A. Muramatsu, Eur. Phys. J. B **17**, 411 (2000)
16. J. Bonča, J.E. Gubernatis, M. Guerrero, E. Jeckelmann, S.R. White, Phys. Rev. B **61**, 3251 (2000)
17. R. Rodríguez-Guzmán, C.A. Jiménez-Hoyos, G.E. Scuseria, Phys. Rev. B **90**, 195110 (2014)
18. M. Lewenstein, A. Sanpera, V. Ahufinger, B. Damski, A. Sen, U. Sen, Adv. Phys. **56**, 243 (2007)
19. T. Esslinger, Annu. Rev. Condens. Matter Phys. **1**, 129 (2010)
20. T. Paiva, Y.L. Loh, M. Randeria, R.T. Scalettar, N. Trivedi, Phys. Rev. Lett. **107**, 086401 (2011)
21. R.A. Hart, P.M. Duarte, T.L. Yang, X. Liu, T. Paiva, E. Khatami, R.T. Scalettar, N. Trivedi, D.A. Huse, R.G. Hulet, Nature **519**, 211 (2015)
22. D. Greif, T. Uehlinger, G. Jotzu, L. Tarruell, T. Esslinger, Science **340**, 1307 (2013)
23. J. Imriška, M. Iazzi, L. Wang, E. Gull, D. Greif, T. Uehlinger, G. Jotzu, L. Tarruell, T. Esslinger, M. Troyer, Phys. Rev. Lett. **112**, 115301 (2014)
24. D. Greif, G. Jotzu, M. Messer, R. Desbuquois, T. Esslinger, Phys. Rev. Lett. **115**, 260401 (2015)
25. Z.Y. Meng, T.C. Lang, S. Wessel, F.F. Assaad, A. Muramatsu, Nature **464**, 847 (2010)
26. S. Sorella, Y. Otsuka, S. Yunoki, Sci. Rep. **2**, 992 (2012)
27. F.F. Assaad, I.F. Herbut, Phys. Rev. X **3**, 031010 (2013)
28. T. Uehlinger, G. Jotzu, M. Messer, D. Greif, W. Hofstetter, U. Bissbort, T. Esslinger, Phys. Rev. Lett. **111**, 185307 (2013)
29. B. Tang, T. Paiva, E. Khatami, M. Rigol, Phys. Rev. Lett. **109**, 205301 (2012)
30. B. Tang, T. Paiva, E. Khatami, M. Rigol, Phys. Rev. B **88**, 125127 (2013)
31. N.D. Mermin, H. Wagner, Phys. Rev. Lett. **17**, 1133 (1966)
32. P.C. Hohenberg, Phys. Rev. **158**, 383 (1967)

33. T. Maier, M. Jarrell, T. Pruschke, M.H. Hettler, Rev. Mod. Phys. **77**, 1027 (2005)
34. S. Fuchs, E. Gull, L. Pollet, E. Burovski, E. Kozik, T. Pruschke, M. Troyer, Phys. Rev. Lett. **106**, 030401 (2011)
35. M. Jarrell, T. Maier, C. Huscroft, S. Moukouri, Phys. Rev. B **64**, 195130 (2001)
36. A. Georges, G. Kotliar, W. Krauth, M.J. Rozenberg, Rev. Mod. Phys. **68**, 13 (1996)
37. E. Gull, P. Werner, O. Parcollet, M. Troyer, Europhys. Lett. **82**, 57003 (2008)
38. E. Gull, P. Staar, S. Fuchs, P. Nukala, M.S. Summers, T. Pruschke, T.C. Schulthess, T. Maier, Phys. Rev. B **83**, 075122 (2011)
39. A. Liebsch, W. Wu, Phys. Rev. B **87**, 205127 (2013)
40. W. Wu, A.M.S. Tremblay, Phys. Rev. B **89**, 205128 (2014)
41. L.C. Martin, The Kondo Lattice Model: a Dynamical Cluster Approximation Approach, Ph.D. thesis, Julius-Maximilians-Universität, Würzburg, 2010
42. C. Barber, D. Dobkin, H. Huhdanpaa, ACM Trans. Math. Software **22**, 469 (1996)
43. T.A. Maier, M. Jarrell, Phys. Rev. B **65**, 041104 (2002)
44. D. Greif, M.F. Parsons, A. Mazurenko, C.S. Chiu, S. Blatt, F. Huber, G. Ji, M. Greiner, Science **351**, 953 (2016)
45. V.W. Scarola, L. Pollet, J. Oitmaa, M. Troyer, Phys. Rev. Lett. **102**, 135302 (2009)
46. Q. Zhou, T.L. Ho, Phys. Rev. Lett. **106**, 225301 (2011)
47. M. Dolfi, A. Kantian, B. Bauer, M. Troyer, Phys. Rev. A **91**, 033407 (2015)
48. F. Werner, O. Parcollet, A. Georges, S.R. Hassan, Phys. Rev. Lett. **95**, 056401 (2005)
49. S. Taie, R. Yamazaki, S. Sugawa, Y. Takahashi, Nat. Phys. **8**, 825 (2012)
50. E. Khatami, M. Rigol, Phys. Rev. A **84**, 053611 (2011)
51. J.S. Bernier, C. Kollath, A. Georges, L. De Leo, F. Gerbier, C. Salomon, M. Köhl, Phys. Rev. A **79**, 061601 (2009)
52. L. De Leo, J.S. Bernier, C. Kollath, A. Georges, V.W. Scarola, Phys. Rev. A **83**, 023606 (2011)
53. P.R.C. Kent, M. Jarrell, T.A. Maier, T. Pruschke, Phys. Rev. B **72**, 060411 (2005)
54. A.W. Sandvik, Phys. Rev. Lett. **80**, 5196 (1998)
55. A. Albuquerque, F. Alet, P. Corboz, P. Dayal, A. Feiguin, S. Fuchs, L. Gamper, E. Gull, S. Gurtler, A. Honecker, A. Kozhevnikov, A. Lauchli, S. Manmana, M. Matsumoto, I. McCulloch, F. Michel, R. Noack, G. Pawlowski, L. Pollet, T. Pruschke, U. Schollwock, S. Todo, S. Trebst, M. Troyer, P. Werner, S. Wessel, J. Magn. Magn. Mater. **310**, 1187 (2007)
56. B. Bauer, L.D. Carr, H.G. Evertz, A. Feiguin, J. Freire, S. Fuchs, L. Gamper, J. Gukelberger, E. Gull, S. Guertler, A. Hehn, R. Igarashi, S.V. Isakov, D. Koop, P.N. Ma, P. Mates, H. Matsuo, O. Parcollet, G. Pawlowski, J.D. Picon, L. Pollet, E. Santos, V.W. Scarola, U. Schollwock, C. Silva, B. Surer, S. Todo, S. Trebst, M. Troyer, M.L. Wall, P. Werner, S. Wessel, J. Stat. Mech. **2011**, P05001 (2011)
57. J. Kuneš, Phys. Rev. B **83**, 085102 (2011)